This is a repository copy of *Two-dimensional elastoplastic analysis of cylindrical cavity problems in Tresca materials*.

White Rose Research Online URL for this paper:
http://eprints.whiterose.ac.uk/145022/

Version: Accepted Version

Article:

Two-dimensional elastoplastic analysis of cylindrical cavity problems in Tresca materials

Pei-Zhi Zhuang*, Hai-Sui Yu

School of Civil Engineering, Faculty of Engineering, University of Leeds, LS2 9JT Leeds, UK

*Corresponding Author, Email: P.Zhuang@leeds.ac.uk

ABSTRACT:

This paper presents analytical elastic-plastic solutions for static stress loading analysis and quasi-static expansion analysis of a cylindrical cavity in Tresca materials, considering biaxial far-field stresses and shear stresses along the inner cavity wall. The two-dimensional static stress solution is obtained by assuming that the plastic zone is statically determinate and using the complex variable theory in the elastic analysis. A rigorous conformal mapping function is constructed, which predicts that the elastic-plastic boundary is in an elliptic shape under biaxial in-situ stresses and the range of the plastic zone extends with increasing internal shear stresses. The major axis of the elliptical elastic-plastic boundary coincides with the direction of the maximum far-field compression stress. Furthermore, considering the internal shear stresses, an analytical large-strain displacement solution is derived for continuous cavity expansion analysis in a hydrostatic initial stress filed. Based on the derived analytical stress and displacement solutions, the influence of the internal shear stresses on the quasi-static cavity expansion process is studied. It is shown that additional shear stresses could reduce the required normal expansion pressure to a certain degree, which partly explains the great reduction of the axial soil resistance due to rotations in rotating cone penetration tests. In addition, through additionally considering the potential influences of biaxial in-situ stresses and shear stresses generated around the borehole during drillings, an improved cavity expansion approach for estimating the maximum allowable mud pressure of horizontal directional drillings (HDDs) in undrained clays is proposed and validated.

Keywords: cavity expansion, conformal mapping function, shear stress, biaxial in-situ stresses, rotating cone penetration test, horizontal directional drilling

1 | INTRODUCTION

Cavity expansion theory has been extensively applied in various fields of geotechnical engineering such as interpretation of cone penetration tests (CPTs), prediction of soil resistance experienced by plate anchors and piles, stability analysis of tunnels and boreholes (e.g. blow out failure associated with loading and local collapse associated with unloading) [1-6]. These successful applications greatly stimulated the development of analytical cavity expansion solutions over the past decades. It is noted that analytical elastic-plastic solutions, in general, have been derived by assuming that the cavity is uniformly loaded by increasing internal normal pressures in a hydrostatic initial stress field. In reality, however, the in-situ soil stresses are not uniform in most cases, and the horizontal earth pressure at rest is often expressed as K_0 times of that in the vertical direction instead (i.e. $\sigma_{h0} = K_0 \sigma_{v0}$) [7, 8]. Meanwhile, a great amount of shear stress might be applied or generated around the inner cavity wall in the process of rotary drilling/excavation, accommodation of screw piles or rotating penetration tests [9-13]. It has been reported that the biaxial in-situ stresses (K_0 effect) and internal shear stresses need to be additionally taken into account for further improving the accuracy of the cavity expansion theory in many applications [13-16], for example, in estimating the tip resistance of rotating CPTs and predicting the maximum mud pressure of HDDs, in particular, at relatively shallow depths [17-19]. To account for the additional influences of these two factors during loading/expansion of a cylindrical cavity in undrained clays, both static stress analysis and quasi-static expansion analysis adopting the linear elastic-perfectly-plastic Tresca model are carried out in this paper.

The stress field developed around a cavity primarily depends on the material strength and imposed boundary conditions. For a cavity with axisymmetric geometry and stress conditions, the stress analysis usually can be simplified to a one-dimensional equilibrium problem, which facilitated the development of a number of analytical elastic and elastic-plastic solutions [1]. When non-axisymmetric geometry and/or stress boundary conditions are considered, more advanced mathematical techniques such as the complex variable theory [20, 21], perturbation methods [22, 23], variational approaches [24] and numerical techniques [25, 26] tend to be required. Among these methods, the complex variable theory in conjunction with the conformal mapping technique provides a very powerful analytical tool for the elastic analysis

28   around a cavity with various boundary conditions [20, 27]. This method has also been extended to the

29   analysis of a cylindrical cavity surrounded by strain-hardening materials obeying the power-law [28, 29].

30   However, these methods cannot be directly applied to the analysis in materials characterised by elastic-

31   perfectly plastic models since the difference between elastic and plastic constitutive equations. To

32   address this problem, Galin [30] creatively proposed an analytical approach for the analysis of a circular

33   cavity embedded in an infinite plate under biaxial remote stretching loadings. By assuming that the

34   plastic zone is statically determinate and using the complex variable theory in the elastic analysis, both

35   constant and polynomial types of far-field stresses were studied by Galin [30]. Although minor mistakes

36   existed in these solutions as found and improved by Ochensberger, et al. [31] and Tokar [32] respectively, it

37   is generally believed that this methodology greatly facilitated the development of analytical/semi-

38   analytical solutions for the two-dimensional elastic-plastic analysis of a series of problems with similar

39   boundary conditions [33-38].

40   Comparing with the problem of Galin [30], uniform shear stresses at the inner cavity wall are additionally

41   considered in this study. As a consequence, Galin's [30] approach to establishing the conformal mapping

42   function cannot be applied to deal with this problem since the plastic state is no longer biharmonic [37].

43   Although Parasyuk [37] has given the form of the conformal mapping function for this problem (see

44   Appendix B) based on Harnack's theorem, the mapping function has not been completely determined.

45   Consequently, the range of the plastic zone is not known, and the elastic field cannot be obtained. In

46   order to give a complete solution to this problem, the conformal mapping function is further explored

47   by introducing Laurent decomposition theorem in the analysis of stress continuity conditions across the

48   elastic-plastic boundary, and closed-form Kolosov-Muskhelishvili complex potentials [20] for the elastic

49   analysis are then derived by using a Fourier series and the Cauchy integral method in this paper. This

50   analytical stress solution is validated by comparing with the finite element method and Galin's [30]

51   solution.

52   To further demonstrate the necessity and importance of considering the internal shear stresses and/or

53   biaxial in-situ stresses in practical geotechnical problems, the newly derived static stress solution and

54 quasi-static expansion solution are applied to estimate the normal soil resistance experienced by a

55 vertically advancing cone with rotations and predict the maximum mud pressure during HDDs:

56 (1) The axial penetration resistance could be significantly reduced by rotations [9, 18, 19]. Therefore, rotating

57 a pushing cone penetrometer is regarded as one of the most feasible physical methods to eliminate the

58 interface friction in modelling the root tip-soil interaction (lubricated interface due to the sloughing off

59 of border cells and mucilage from roots) [9, 11, 18]. In rotating CPTs, shear stresses would be generated

60 around the sliding interface, which not only decrease the frictional resistance both on the cone tip and

61 the shaft and may also lead to additional plastic failure in the surrounding soil [18, 19]. The reduction of the

62 axial tip resistance is usually attributed to the reorientation of the frictional resistance at the cone and

63 the additional plastic deformation caused by the generated shear stresses [18, 19]. The former effect has

64 been explained by Bengough, et al. [18] based on quasi-static equilibrium analysis. Unfortunately,

65 analytical methods accounting for the latter effect are still rarely available. According to the analogy of

66 cone penetration and continuous expansion of a cylindrical cavity [39, 40], an analytical quasi-static

67 expansion solution is developed to capture the additional influences of cone rotations on the normal soil

68 resistance in this paper.

69 (2) HDD becomes a popular alternative to traditional open-cut excavation for pipeline and underground

70 utility conduit installation due to its higher flexibility in operation and potential economic and

71 environmental benefits [41-43]. During HDDs, it requires continuous circulation of pressurized fluid in the

72 bore to remove the cutting out, stabilize the bore formation, cool and clean the drill bit, and lubricate

73 the pipe during installation. To avoid inadvertent drilling fluid returns and also effectively return the

74 soil cutting from the boring path to the ground surface, the determination or control of the applied

75 drilling fluid pressure remains a serious concern in the design and implementation of HDDs, especially

76 the maximum allowable mud pressure [44-46]. Cylindrical cavity expansion solutions provide one of the

77 most commonly used theoretical methods for estimating the maximum mud pressure during HDDs [5, 17,

78 [42, 47], for example, the Delft cylindrical cavity expansion model (Delft solution) proposed by Luger and

79 Hergarden [48] by extending Vesic's solution [49]. In the Delft solution, the in-situ stress field is simplified

80 to be hydrostatic [5, 47]. However, for HDD practices implemented at relatively shallow depths, it has been

81 reported that the K_0 effect may exert significant influences on the maximum allowable mud pressure [17,

82 50]. Considering the K_0 effect, Xia and Moore [17] proposed an approximate method by replacing the elastic

83 stresses in the Delft solution with Kirsch equations (i.e. m=0 in Appendix A) while estimating the

84 maximum mud pressure in undrained clays. However, the elastic and plastic stresses were derived

85 independently in their solution, and the elastic-plastic boundary was assumed to be circular regardless

86 of the biaxial in-situ stresses. By using the more rigorous stress solution derived in this paper, the

87 method of accounting for the K_0 effect is further improved. Meanwhile, the shear stresses potentially

88 generated during pilot hole boring and reaming of HDDs are also considered in the new method.

89 **2 | PROBLEM DEFINITION**

90 A sufficiently large and thick soil medium (in comparison with the cavity size) with an inside cylindrical

91 cavity is considered. As depicted in Figure 1, biaxial initial stresses apply at infinity, and uniform shear

92 stresses act on the inner cavity wall. The surrounding medium is loaded monotonically by normal

93 compression pressures on the inner cavity wall to the value of p_{in} with a sufficiently slow speed. The

94 stress and deformation analysis are conducted under the assumption of plane strain. For convenience,

95 both Cartesian coordinates (x, y, z) and cylindrical polar coordinates (r, θ, z) with the same origin at the

96 centre of the cavity are utilised. It is worth noting that the defined remote stress conditions are

97 sufficiently general because we always can set a coordinate system with axes parallel to the directions

98 of the principal stresses at infinity. Within the cylindrical polar coordinates, the stress equilibrium

99 equations in the radial and circumferential directions, respectively, are

100
$$\frac{\partial \sigma_r}{\partial r} + \frac{1}{r}\frac{\partial \tau_{r\theta}}{\partial \theta} + \frac{\sigma_r - \sigma_\theta}{r} = 0 \tag{1}$$

101
$$\frac{1}{r}\frac{\partial \sigma_\theta}{\partial \theta} + \frac{\partial \tau_{r\theta}}{\partial r} + \frac{2\tau_{r\theta}}{r} = 0 \tag{2}$$

102 where σ_r, σ_θ and $\tau_{r\theta}$ are the radial, circumferential and shear stress components, respectively.

103 Taking tension as positive for normal stresses and rotation in the anticlockwise direction to the object

104 as positive for shear stresses, the stress boundary conditions can be expressed as

5

105 $\left.\sigma_r\right|_{r=R} = -p_{in}$, $\left.\tau_{r\theta}\right|_{r=R} = mk$ ($-1 \leq m \leq 1$) (3)

106 $P_\infty = (\left.\sigma_y\right|_{y\to\infty} + \left.\sigma_x\right|_{x\to\infty})/2 = -(\sigma_{v0} + \sigma_{h0})/2$, $\tau_\infty = (\left.\sigma_y\right|_{y\to\infty} - \left.\sigma_x\right|_{x\to\infty})/2 = (\sigma_{h0} - \sigma_{v0})/2$ (4)

107 where k is the yield stress under pure shear loading. m gives the relationship between k and the

108 internal shear stress.

109 The surrounding material is regarded as homogenous and isotropic, and it is characterised with an

110 elastic-perfectly plastic model. Specifically, the elastic response is described by Hooke's law until the

111 onset of yielding which obeys the Tresca yield criterion (i.e. Equation 5).

112 $\left(\sigma_r - \sigma_\theta\right)^2 + 4\tau_{r\theta}^2 = 4k^2$ (5)

113 **3 | STATIC STRESS ANALYSIS**

114 **3.1 | Plastic region**

115 As an extension of Galin's [30] solution, this solution aims to provide an analytical method for the static

116 stress analysis of the soil around a cavity under conditions of: (a) the inner cavity is fully enclosed by a

117 connected plastic region, and the plastic stress field is statically determinate, (b) the plastic zone is

118 developed under monotonic loading, and no elastic unloading occurs in any case, and (c) the out-of-

119 plane stress component σ_{zz} always remains as the intermediate principal stress regardless of other

120 stresses [33, 35].

121 The static determinacy of the plastic field determines that the plastic stress field entirely depends on the

122 inner boundary conditions [35, 51]. Therefore, according to the axisymmetric fact of the geometry and stress

123 boundaries at the inner cavity wall, it is reasonable to assume

124 $\dfrac{\partial \sigma_r^p}{\partial \theta} = 0$, $\dfrac{\partial \sigma_\theta^p}{\partial \theta} = 0$, $\dfrac{\partial \tau_{r\theta}^p}{\partial \theta} = 0$ (6)

125 where the superscripts [e] and [p] indicate the stress components in the elastic and plastic region respectively.

126 The plastic stresses under loading can be obtained by solving the stress equilibrium equation (i.e.

127 Equation 3) and the yield criterion (i.e. Equation 5) with the given stress boundaries (i.e. Equation 3),

128 which are known as the Mikhlin's solution [13, 37] (i.e. Equations 7-9).

6

129 $$\sigma_r^p = k \left\langle \ln\left[\frac{(r/R)^2 + \sqrt{(r/R)^4 - m^2}}{1 + \sqrt{1 - m^2}} \right] - \sqrt{1 - m^2 (\frac{R}{r})^4} + \sqrt{1 - m^2} \right\rangle - p_{in}$$ (7)

130 $$\sigma_\theta^p = k \left\langle \ln\left[\frac{(r/R)^2 + \sqrt{(r/R)^4 - m^2}}{1 + \sqrt{1 - m^2}} \right] + \sqrt{1 - m^2 (\frac{R}{r})^4} + \sqrt{1 - m^2} \right\rangle - p_{in}$$ (8)

131 $$\tau_{r\theta}^p = mk \frac{R^2}{r^2}$$ (9)

3.2 | Determination of conformal mapping function

133 The elastic-plastic interface gives the outer boundary of the plastic zone and simultaneously provides

134 the inner boundary for computing the elastic stress field, which is, therefore, of great importance for

135 determining the range of the developed plastic zone and deriving the elastic stresses. The location of

136 the elastic-plastic boundary is generally determined by analysing the continuity conditions of the elastic

137 and plastic stresses across the interface. However, under non-equal far-field stresses, the elastic stress

138 field cannot be obtained prior to knowing its inner boundary conditions, namely the location of the

139 elastic-plastic boundary and stresses acting on it [30, 33, 35, 37]. Therefore, the elastic-plastic boundary is

140 described by a general form of the conformal mapping function first (i.e. Equation B1), and the elastic

141 stresses are represented in terms of general forms of Kolosov-Muskhelishvili complex potentials, $\Phi(\zeta)$

142 and $\Psi(\zeta)$ [20]. Based on the stress continuity conditions across the elastic-plastic boundary and the far-

143 field stress boundary conditions, the boundary values of $\Phi(\zeta)$ and $\Psi(\zeta)$ can be expressed as

144 $$\Phi(\zeta) + \overline{\Phi(\zeta)} = \frac{(\sigma_r^e + \sigma_\theta^e)}{2}$$
$$= \begin{cases} k \left\langle \ln\left[\frac{\omega(\sigma)\overline{\omega(\sigma)}/R^2 + \sqrt{[\omega(\sigma)\overline{\omega(\sigma)}]^2/R^4 - m^2}}{1 + \sqrt{1 - m^2}} \right] + \sqrt{1 - m^2} \right\rangle - p_{in} & ,\text{at } \gamma \quad (a) \\ P_\infty & ,\zeta \to \infty \ (b) \end{cases}$$ (10)

145 $$\frac{\overline{\omega(\zeta)}}{\omega'(\zeta)} \Phi'(\zeta) + \Psi(\zeta) = \frac{(\sigma_\theta^e - \sigma_r^e + 2i\tau_{r\theta}^e)}{2} e^{-2i\theta}$$
$$= \begin{cases} k \left\langle \frac{\sqrt{[\omega(\sigma)\overline{\omega(\sigma)}]^2 - m^2 R^4} + mR^2 i}{\omega(\sigma)\overline{\omega(\sigma)}} \right\rangle \frac{\overline{\omega(\sigma)}}{\omega(\sigma)} & ,\text{at } \gamma \quad (a) \\ \tau_\infty & ,\zeta \to \infty \ (b) \end{cases}$$ (11)

146   where $i = \sqrt{-1}$. γ represents the unit contour in the phase plane, corresponding to the elastic-plastic

147   boundary. σ is the unit complex variable, which describes points on γ. $\sigma = \cos\phi + i\sin\phi = e^{i\phi}$. and

148     $\bar{\sigma} = 1/\sigma$. ϕ is the argument of σ. The function of $\omega(\zeta)$ conformally maps the exterior of the elastic-

149   plastic boundary in the physical plane onto the exterior region of the unit circle in the phase plane;

150     $\overline{\omega(\zeta)}$ is its conjugate function. $\zeta = \xi + i\eta = \rho e^{i\phi}$. ξ and η are the real and imaginary part of the

151   complex variable ζ, respectively. ρ is the modulus of ζ. Boundary conditions of Equation 10b and

152   Equation 11b specified the behaviour of the complex potentials at infinity as

153     $$\Phi(\infty) = \frac{P_\infty}{2} + O(\zeta^{-2}) \quad , \quad \Psi(\infty) = \tau_\infty + O(\zeta^{-2}) \tag{12}$$

154   Owing to the additional consideration of the internal shear stresses, the plastic state is no longer

155   biharmonic. Thus the mapping function cannot be determined by constructing a unified biharmonic

156   stress function crossing the elastic-plastic interface as proposed by Galin[30]. Instead, Equations 10 and

157   11 are analysed based on Harnack's theorem. With this method, the form of the mapping function (i.e.

158   Equation 13) was derived by Parasyuk[37], and a more general derivation is presented in Appendix B.

159     $$\omega(\zeta) = \alpha(\zeta + \frac{\beta}{\zeta}) \tag{13}$$

160   where $\beta = \tau_\infty / k$.

161   Equation 13 gives that the elastic-plastic boundary is in an elliptic shape while $\beta \neq 0$, whose major axis

162   is along the direction of the maximum far-field compression pressure under loading. However, the

163   parameter α in Equation 13 has not been determined so far. Consequently, the range of the plastic zone

164   and elastic stresses cannot be analytically obtained. To derive a complete solution to this problem,

165   Equations 10 and 11 are further analysed as follows.

166   As the far-field stress conditions bound the behaviour of the right-hand side of Equation 10a at infinity

167   [27, 52], the continuity condition of the mean stress can be re-expressed as

168     $$\Phi(\sigma) + \overline{\Phi(\sigma)} = k\ln[F(\sigma,\bar{\sigma})] + k\sqrt{1-m^2} - p_{in} \tag{14}$$

169   where $F(\sigma,\bar{\sigma}) = \left\{ \dfrac{\omega(\sigma)\overline{\omega(\sigma)}/R^2 + \sqrt{[\omega(\sigma)\overline{\omega(\sigma)}]^2/R^4 - m^2}}{(1+\sqrt{1-m^2})\sigma\bar{\sigma}} \right\} = \dfrac{f(\sigma)}{\sigma} \dfrac{\bar{f}(\bar{\sigma})}{\sigma^{-1}}$.

170   An elliptic elastic-plastic boundary is predicted by Equation 13, which is a closed smooth contour in

171   the physical plane. $\ln[F(\sigma,\bar{\sigma})]$ in Equation 14 continues analytically on both sides of γ in an annulus

172   of $0 \le |\zeta - \sigma| \le \infty$. Thus, based on Laurent decomposition theorem [53], $\ln[F(\sigma,\bar{\sigma})]$ can be decomposed

173   as a sum of two mutually conjugate functions, $d(\zeta)$ and $\bar{d}(\zeta^{-1})$, which are analytic in Ω^+ ($|\zeta| < 1$)

174   and Ω^- ($|\zeta| > 1$) respectively. Then by multiplying $\dfrac{1}{2\pi i}\dfrac{d\sigma}{\sigma - \zeta}$ on both sides of Equation 14 and

175   integrating it along γ, we obtain

176      $F^+(\zeta) = \bar{d}(\zeta^{-1}) - \overline{\Phi(\zeta)}$ (15 a)

177      $F^-(\zeta) = \Phi(\zeta) - d(\zeta) - (k\sqrt{1-m^2} - p_{in})$ (15 b)

178   where $d(\zeta) = k\ln[f(\zeta)/\zeta]$ and $\bar{d}(\zeta^{-1}) = k\ln[f(\bar{\zeta})/\zeta^{-1}]$. $F^+(\zeta)$ and $F^-(\zeta)$ are analytic

179   everywhere within the region of Ω^+ and Ω^-, respectively. Now the continuity condition of the mean

180   stress across the unit circle γ can be expressed as $F^+(\sigma) = F^-(\sigma)$. Based on Liouville's theorem,

181   which states $F^+(\zeta)$ and $F^-(\zeta)$ are identically equal to one and same constant due to the complex

182   potentials are bounded at infinity. The boundary values of $d(\zeta)$ and $\bar{d}(\zeta^{-1})$ are studied in the

183   extended complex plane with the form defined in Equation 14. By analysing Equation 14, it is obtained

184   that

185      $-\dfrac{P_\infty}{2} + \dfrac{1}{2}k\ln[\dfrac{2\alpha^2/R^2}{1+\sqrt{1-m^2}}] = \dfrac{P_\infty}{2} - \dfrac{1}{2}k\ln(\dfrac{2\alpha^2/R^2}{1+\sqrt{1-m^2}}) - k\sqrt{1-m^2} + p_{in}$ (16)

186   As a result, the undetermined parameter α in Equation 13 is obtained as

187      $\alpha = \delta Re^{\frac{1}{2k}[p_{in} + P_\infty - k\sqrt{1-m^2}]}$ (with $\delta = \left[(1+\sqrt{1-m^2})/2\right]^{1/2}$)   (17)

188   By now the conformal mapping function is completely determined. A new parameter δ is involved

189   due to the additional consideration of the internal shear stresses comparing with Galin's [30] mapping

190   function. Equation 17 indicates that the size of the plastic region monotonically expands with an

191   increasing expansion pressure. The lengths of the semi-major axis and the semi-minor axis of the elliptic

192   elastic-plastic boundary can be expressed as $a_{ep} = \alpha(1+|\beta|)$ and $b_{ep} = \alpha(1-|\beta|)$ respectively. It is

193   shown that the axis ratio (a_{ep} / b_{ep}) and axes directions of the elastic-plastic boundary entirely depend

194   on the non-uniformity of far-field stresses (represented by the non-dimensional factor of β).

3.3 | Elastic stress analysis

196   The derived elastic-plastic boundary and plastic stresses provide the inner geometry and stress

197   boundaries for the analysis of the outside elastic field. In other words, now the elastic field is equivalent

198   to the problem that an elliptic cavity embedded in an infinite plane subjecting to non-uniform stresses

199   at the inner cavity wall and biaxial stresses at infinity. At first, the elastic stresses are represented by

200   the general forms of the elastic complex potentials (i.e. Equations 18 and 19) according to the complex

201   potential method proposed by Muskhelishvili [20].

202    $$\Phi(\zeta) = \Gamma - \frac{X+iY}{2\pi(1+\chi)}\frac{1}{\zeta} + \Phi_0(\zeta) \tag{18}$$

203    $$\Psi(\zeta) = \Gamma' + \frac{\chi(X-iY)}{2\pi(1+\chi)}\frac{1}{\zeta} + \Psi_0(\zeta) \tag{19}$$

204   where $\Phi_0(\zeta) = \sum_{n=1}^{\infty}\frac{a_n}{\zeta^{n+1}}$, $\Psi_0(\zeta) = \sum_{n=1}^{\infty}\frac{b_n}{\zeta^{n+1}}$, which are holomorphic in the whole elastic region.

205    $\Gamma = P_{\infty} / 2$ and $\Gamma' = \tau_{\infty}$, which describe the stress conditions at infinity. X and Y are components of the

206   resultant vector of forces acting on the elastic-plastic boundary. $\chi = 3-4\nu$ for the plane strain problem.

207   ν is Poisson's ratio.

208   The complex potentials are first sought with the assumption that both the stress and displacement

209   components remain bounded at infinity, which implies that the resultant stresses vanish at infinity [20].

210   Mathematically, it requires $\Gamma = \Gamma' = 0$ and $X = Y = 0$. In this case, the complex potentials remain

211   holomorphic in the outside region of contour γ . $\Phi_0(\zeta)$ and $\Psi_0(\zeta)$ fully satisfy the above

212   requirements. According to the stress boundary conditions at the elastic-plastic boundary given in

213 Equations 10 and 11, it is not easy to derive the elastic complex potentials directly with simple algebraic

214 transformations, if possible. Alternatively, the inner stress boundaries of the mean stress (i.e. Equation

215 10a) are transformed into a Fourier series form as

216
$$\Phi_0(\sigma) + \overline{\Phi_0(\sigma)} = k \ln\left[\frac{(x_{ep}^2 + y_{ep}^2)/R^2 + \sqrt{(x_{ep}^2 + y_{ep}^2)^2/R^4 - m^2}}{1 + \sqrt{1 - m^2}}\right] + k\sqrt{1 - m^2} - p_{in} - P_\infty$$
$$= G(\phi) = \sum_{-\infty}^{+\infty} A_n e^{in\phi} = \sum_{-\infty}^{+\infty} A_n \sigma^n$$
(20)

217 where $A_n = \dfrac{1}{2\pi}\displaystyle\int_0^{2\pi} G(\phi)e^{-in\phi}d\phi$. $x_{ep} = \alpha(1 + \beta)\cos\phi$ and $y_{ep} = \alpha(1 - \beta)\sin\phi$.

218 In Equation 20, an even function of $G(\phi)$ is formed, which is a continuous real function in terms of the

219 argument ϕ within the interval of $0 \leq \phi \leq 2\pi$. It means that $A_n = A_{-n}$ (real numbers) and coefficients

220 of the odd terms in $\Phi_0(\sigma)$ are infinitesimal. As $A_{-n} = \overline{A_n}$ and $\bar\sigma = \sigma^{-1}$, naturally both sides of Equation

221 20 can be split into two mutually conjugate parts. As a result,

222 $$\Phi_0(\sigma) = A_0/2 + \sum_{n=1}^{+\infty} A_{-2n}/\sigma^{2n}$$
(21)

223 As A_0 is vanishingly small, the requirement of $\Phi_0(\sigma)$ at infinity, namely $\Phi_0(\infty) = O(\zeta^{-2})$, is fulfilled.

224 More strictly in the mathematical formulation, the term with coefficients of A_0 in Equation 21 is

225 equivalently modified at the unit circle as

226 $$\Phi_0(\sigma) + \overline{\Phi_0(\sigma)} = \sum_{n=1}^{+\infty} A_{-2n}\frac{1}{\sigma^{2n}} + \frac{A_0}{2|\sigma|^2} + \frac{A_0}{2}|\sigma|^2 + \sum_{n=1}^{+\infty} A_{2n}\sigma^{2n}$$
(22)

227 By multiplying both sides with $\dfrac{1}{2\pi i}\dfrac{d\sigma}{\sigma - \zeta}$ (here ζ is a point within Ω^-) and then integrating it along

228 the circumference of γ, Equation 22 gives

229 $$\Phi_0(\zeta) = \frac{A_0}{2|\zeta|^2} + \sum_{n=1}^{+\infty} \frac{A_{-2n}}{\zeta^{2n}}$$
(23)

230 Then the general form of $\Phi(\zeta)$ can be obtained by releasing the previous assumption in the process of

231 deriving $\Phi_0(\sigma)$. The resultant vectors still equal to zero ($X = Y = 0$) because of the continuous

232   distribution of stresses along the elastic-plastic boundary. With the use of Equation 12 and 23, the first

233   complex potential goes to

234     $$\Phi(\zeta) = \frac{P_\infty}{2} + \Phi_0(\zeta) \qquad (24)$$

235   Then the complex potential $\Psi(\zeta)$ is derived by integrating the continuity condition of the deviatoric

236   stress (i.e. Equation 11a) along γ from the side of Ω^- with the Cauchy integral method. As discussed

237   in Appendix B, all terms in Equation 11a are holomorphic in Ω^-, therefore $\Psi(\zeta)$ goes to

238     $$\Psi(\zeta) = k\frac{(\beta\zeta^2 + 1)}{(\zeta^2 + \beta)}\left\langle \frac{\sqrt{\hat{r}^4 - m^2 R^4} + mR^2 i}{\hat{r}^2}\right\rangle - \frac{\zeta(\beta\zeta^2 + 1)}{\zeta^2 - \beta}\Phi'(\zeta) \qquad (25)$$

239   where $\hat{r}^2 = \alpha^2(1 + \beta^2 + \beta\zeta^2 + \beta\zeta^{-2})$. $\Phi'(\zeta)$ is the derivative of the complex potential $\Phi(\zeta)$ with

240   respect to ζ, which can be easily calculated with $|\zeta|^2 = \xi^2 + \eta^2$ and $\frac{\partial}{\partial\zeta} = \frac{1}{2}(\frac{\partial}{\partial\xi} - i\frac{\partial}{\partial\eta})$. Hence,

241     $$\Phi'(\zeta) = -\frac{A_0}{2\zeta|\zeta|^2} - \sum_{n=1}^{+\infty} 2n\frac{A_{-2n}}{\zeta^{2n+1}} \qquad (26)$$

242   Now this stress boundary value problem is analytically solved through the combination use of the

243   Cauchy integral method and Fourier series as shown in Equations 23-26.

4 | DISCUSSION ON RESTRICTIONS FROM THE ASSUMPTIONS

245   As stated in Section 3.1, the above static stress solution was derived based on several prior assumptions.

246   Restrictions due to these assumptions are discussed as follows.

247   (1) The cavity is fully enclosed by a plastic region

248   This assumption requires that the inner cavity is fully enclosed by a continued plastic region. Limit

249   conditions of this requirement will be approached while the vertices of the predicted elastic-plastic

250   boundary in the minor axis direction just reach the cavity wall [33]. It gives

251     $$b_{ep} = \alpha(1 - |\beta|) \geq R \qquad (27)$$

252   (2) Intermediate principal stress

253 It was assumed that the out-of-plane stress σ_{zz} always remains as the intermediate principal stress.

254 Although this assumption is always justified for incompressible conditions, restrictions will be

255 produced in compressible materials. The plastic stress solutions show that the principal stresses in the

256 plastic zone vary from the inner cavity wall to the elastic-plastic boundary monotonically. Therefore, it

257 just needs to ensure that values of σ_{zz} at the inner cavity wall and at the vertices on the major axis of

258 the elastic-plastic boundary always remain as the intermediate principal stress [33]. Relationships between

259 the principal stresses and other stress components are given in Appendix A. With the aid of Equations

260 7, 8, and 9, this restriction for compressible Tresca materials can be expressed as

261
$$\sqrt{1-m^2} - \frac{1}{1-2\nu} + \ln(\Theta) \le \frac{p_{in}}{k} \le \sqrt{1-m^2} + \frac{1}{1-2\nu} \tag{28}$$

262 where $\Theta = \dfrac{[\alpha(1+|\beta|)/R]^2 + \sqrt{[\alpha(1+|\beta|)/R]^4 - m^2}}{1+\sqrt{1-m^2}} > 1$.

263 (3) Static determinacy of the plastic zone

264 The plastic stresses were derived by assuming that the plastic zone is statically determinate.

265 Theoretically, it implies that every point in the plastic region can be connected to the cavity rim by two

266 characteristic lines (slip-lines) of different families, and every slip-line cuts the elastic-plastic boundary

267 only once [51]. Therefore, the limit condition will be reached while one, and only one, characteristic line

268 is tangent to the elastic-plastic interface within one quadrant.

269 It is known that directions of the slip-lines take an angle of $\pi/4$ with the principal stress directions in

270 Tresca materials. While internal shear stresses apply, the radial and circumferential directions are no

271 longer the principal stress directions in the plastic zone. As shown in Figure 2, the direction of the minor

272 principal stress takes an anticlockwise rotation to the radial direction of the cylindrical coordinates with

273 positive shear stresses at the inner cavity wall. Contrarily, a clockwise rotation would be caused by

274 negative shear stresses. Here taking the anticlockwise direction of φ as positive, according to Figure

275 3, the requirement of this assumption can be expressed as

276
$$|\lambda - \theta| \le \frac{\pi}{4} + \varphi \tag{29}$$

13

277   where θ is the angle between the radial direction and the x-axis. λ represents the angle between the

278   outward normal to the elastic-plastic interface and the x-axis.

279   Angles in Equation 29 all can be expressed in terms of the unit complex variable σ as

280    $$e^{2i(\lambda-\theta)} = \sigma^2 \frac{\omega'(\sigma)}{\overline{\omega'(\sigma)}} \frac{\overline{\omega(\sigma)}}{\omega(\sigma)} = \frac{(\sigma^2-\beta)}{(1-\beta\sigma^2)} \frac{(1+\beta\sigma^2)}{(\beta+\sigma^2)} \quad ; \quad 2\varphi = \arcsin\left[m \frac{R^2}{\omega(\sigma)\overline{\omega(\sigma)}} \right] \qquad (30)$$

281   where $\omega(\sigma) = \alpha(\sigma + \beta\sigma^{-1})$; $\overline{\omega(\sigma)} = \alpha(\sigma^{-1} + \beta\sigma)$.

282   To ensure that only one characteristic line reaches the limit condition within one quadrant, it restricts

283   that the equality condition holds only when the function $g(\sigma) = |\lambda-\theta| - \varphi$ reaches its extremum [35]. The

284   extremum values of $g(\sigma)$ lie at the zero points of its first derivative. If no shear stress is applied, this

285   restriction becomes $|\beta| \leq (\sqrt{2}-1)$ [33, 35].

286   With the defined boundary conditions, stress states developed around the inner cavity can be broadly

287   categorized into three conditions [26, 33]: a) purely elastic state (i.e. zone A); b) the cavity is partially

288   surrounded by plastic regions (e.g., zone B and zone E); and c) the cavity is fully enclosed by a plastic

289   region (e.g. zone C and zone D). The stress field in a purely elastic state can be readily calculated with

290   the solution given in Appendix A. The limit pressure that a plastic zone starts forming from the inner

291   cavity wall under loading is useful in estimating the plastic initiation pressure of fracturing [14], and,

292   therefore, it is also given in Equation 31.

293    $$(p_{in} + P_{\infty}) \geq k\sqrt{1-m^2} - 2|\tau_{\infty}| \qquad (31)$$

294   In the other two stress states, distributions of the plastic regions are various, mainly depending on the

295   material strength and boundary conditions [26, 33]. By using Equations 27-31, example boundaries of

296   different stress states are shown in Figure 4 for illustration. As previously discussed, the present solution

297   is dedicated to problems with boundary stresses belonging to Zone C.

298   Without the internal shear stresses, Figure 4 shows that Equations 27-31 give the same results as that

299   given by Yarushina et al. [33] for the problem of Galin [30], and the distribution patterns of the plastic regions

300   in Zones D and E refer to Yarushina et al. [33]. When additional shear stresses apply, the limits of different

301   stress states would change. In specific, Line 2 (representing the limit given by Equation 27) moves

302   leftwards with increasing shear stresses. Line 3 (determined by Equation 29) represents the limit of

303   static determinacy of the plastic region. It is a horizontal line with a constant value of $|\beta| \leq (\sqrt{2}-1)$ in

304   the case without internal shear stresses, but becomes curved due to the rotation of principal stresses

305   caused by the internal shear stresses. Opposite rotations will be produced by the shear stresses with

306   different applying directions. As a result, the bounds of this requirement distribute in opposite sides of

307   the horizontal line of $|\beta| \leq (\sqrt{2}-1)$, but they both gradually approach to $(\sqrt{2}-1)$ with an increasing

308   value of $|P_{\infty} + p_{in}|/k$. Line 4 reflects the restriction specified by Equation 28. The additional shear

309   stresses exert little impact on this restriction. Example lines calculated with $p_{in} = 0$ and $\nu = 0.4$ are

310   shown in Figure 4. Line 4 moves rightwards (or leftwards) with an increasing (or decreasing) Poisson's

311   ratio, and this restriction will be released in incompressible materials.

312   5 | SOLUTION VALIDATION AND DISCUSSION

313   Within the permissible stress states specified by Equations 27, 28, and 29, the above solution for static

314   stress analysis under loading can be calculated with the following steps.

315   (a) determine the elastic-plastic boundary by using the mapping function given in Equation 13. Then

316   the plastic stress field can be obtained from Equations 7, 8, and 9 directly. One-to-one corresponding

317   relations between the physical plane and the phase plane can be established by using Equation 32;

318   $$x = r\cos\theta = \alpha(\rho + \frac{\beta}{\rho})\cos\phi \ , \ y = r\sin\theta = \alpha(\rho - \frac{\beta}{\rho})\sin\phi \quad\quad (32)$$

319   (b) calculate the coefficients of the established Fourier series (e.g. Equation 23), which stay the same

320   values in the whole elastic filed (setting $n = 5$ in Equation 23 in the following calculations). The elastic

321   complex potentials given in Equations 24 and 25 can then be calculated. By substituting the complex

322   potentials into Equations 33 and 34, stresses in the elastic region can be readily obtained by separating

323   the real and imaginary parts.

324   $$\sigma_x^e + \sigma_y^e = 4\text{Re}[\Phi(\zeta)] \quad\quad (33)$$

15

325 $$\sigma_y^e - \sigma_x^e + 2i\tau_{xy}^e = 2[\frac{\overline{\omega(\zeta)}}{\omega'(\zeta)}\Phi'(\zeta) + \Psi(\zeta)] \qquad (34)$$

5.1 | Comparison with Galin's solution and finite element method

327 The analytical solution is validated by comparing with Galin's [30] solution (i.e. the special case of zero

328 internal shear stress) and the finite element method (FEM) as shown in Figures 5 and 6 respectively.

329 The FEM simulations are implemented in Abaqus/Standard 6.12 using the same linear elastic-perfectly-

330 plastic Tresca model as the above analytical solution. Biaxial far-field stresses are applied at the outer

331 boundaries (100 times of the cavity radius away from the centre) of the plane-strain FEM model, and

332 the same stress boundary conditions are applied at the inner cavity wall as depicted in Figure 1. An 8-

333 node biquadratic plane-strain quadrilateral element is utilised for meshing.

334 It was introduced that Galin's [30] solution is a special case that without shear stresses on the inner cavity

335 wall of the present solution. Although different methods to decomposing the stress continuity conditions

336 have been adopted in these two solutions, Figure 5 demonstrated that the present solution can fully

337 recover to Galin's [30] solution while taking m=0. When internal shear stresses apply, the analytical

338 predictions are in good agreements with the FEM simulations as shown in Figure 6. It is found that the

339 influence of the additional shear stress mainly concentrates in the plastic region, and the shear stress

340 rapidly attenuates from the boundary value at the cavity wall to a stable level that varies in directions

341 and depends on non-uniformity of the far-field stresses. Overall, it is shown that the developed series-

342 form elastic complex potentials have good convergence precision and speed in computations, and the

343 analytical solution can accurately calculate the surrounding elastic and plastic stress fields in the defined

344 stress state.

5.2 | Distribution of elastic-plastic boundary

346 The range of the plastic zone developed around the inner cavity can be predicted by Equation 13. It is

347 shown in Figure 7 that additional internal shear stresses extend the range of the plastic zone, but it

348 imposes no influence on the shape of the elastic-plastic boundary (the major to minor axis ratio remains

349 unchanged as $a_{ep} / b_{ep} = (1+|\beta|) / (1-|\beta|)$. The major axis of the elliptic elastic-plastic boundary under

16

350   loading lies in the x-axis direction while $\beta > 0$, whereas it is along the y-axis direction while $\beta < 0$.

351   In other words, the direction of the major axis coincides with the direction of the minor principal stress

352   (i.e. maximum compression stress) at infinity.

6 | QUASI-STATIC CAVITY EXPANSION SOLUTION IN A HYDROSTATIC STRESS FIELD

355   As previously discussed, rotations during cone penetrations may cause additional plastic failure in the

356   surrounding soil comparing with non-rotated cone penetrations. It is believed that this effect contributes

357   to the great reduction of the axial soil resistance measured by a rotating penetrometer [18, 19]. Based on the

358   analogy of cone penetration and continuous cavity expansion, cylindrical cavity expansion solutions

359   have been applied to estimate the normal soil pressure acting on non-rotated cones with some successes

360   [39, 40]. In rotating CPTs, a rotating cone displaces the ahead soil increasingly cylindrical [18]. Therefore, a

361   cylindrical quasi-static expansion analysis considering internal shear stresses is developed to account

362   for the impact of the additional plastic deformation on the normal soil resistance measured in rotating

363   CPTs as follows.

364   The quasi-static analysis of a cylindrical cavity models the lateral soil response caused by a vertically

365   advancing cone. The confining in-situ soil stresses in a horizontal plane are assumed to be uniform.

366   With uniform in-situ stresses, the mapping function of the elastoplastic interface (i.e. Equation 13) will

367   reduce to $\omega(\sigma) = \alpha\sigma$. Therefore, the inner pressure during expansion can be expressed as

$$\frac{p_{in} + P_\infty^h}{k} = 2\ln(\frac{r_c^h}{\delta R}) + \sqrt{1 - m^2} \tag{35}$$

369   where r_c^h is the elastic-plastic radius under the corresponding hydrostatic initial stress of P_∞^h.

370   Radial displacements during continuous cavity expansions can be obtained by using the derived large-

371   strain displacement solution in Appendix C. By letting $r = R$ and $r_0 = R_0$ in Equation C8, the radius

372   ratio (r_c^h / R) of the elastic-plastic boundary to the current cavity at any expansion instant can be

373   expressed as Equation 36.

$$374 \quad \left[1-\frac{k}{2G}\sqrt{1-m^2\left(\frac{R}{r_c^h}\right)^4}\right]^2 (\frac{r_c^h}{R})^2 - (\frac{R_0}{R})^2$$

$$= \frac{1}{\varpi^2-1}\left[\left(\frac{(r_c^h/R)^2+\sqrt{(r_c^h/R)^4-m^2}}{1+\sqrt{1-m^2}}\right)^\varpi (1+\varpi\sqrt{1-m^2})-[(\frac{r_c^h}{R})^2+\varpi\sqrt{(\frac{r_c^h}{R})^4-m^2}]\right] \quad (36)$$

375 While regarding the material as incompressible (i.e. $v = 0.5$), the displacement solution of Zhou et al.[13]

376 can be recovered by Equation 36 as:

$$377 \quad \frac{r_c^h}{R} = \sqrt[4]{\left[\frac{G}{k}[(1-(\frac{R_0}{R})^2]\right]^2 + m^2} \quad (37)$$

378 Equation 36 gives that a limit value of r_c^h / R exists during continuous expansions. This limit can be

379 approached by putting $R_0 / R \rightarrow \infty$. In the special case of zero internal shear stress (i.e. $m = 0$), the

380 limit ratio of r_c^h / R given by Yu [1] from a rigorous similarity analysis, considering the material

381 compressibility, can be recovered as given in Equation 38, neglecting the small quantities.

$$382 \quad \frac{r_c^h}{R} = \left[(\varpi-1)(1-\frac{k}{2G})^2+1\right]^{\frac{1}{2(\varpi-1)}} \quad (38)$$

383 A rigorous quasi-static expansion solution is obtained by the combination use of Equations 35 and 36.

384 In the simplified cases of $v = 0.5$ and $m = 0$, the well-known limit expansion pressure derived by

385 Gibson and Anderson [54] (i.e. Equation 39) can be recovered by substituting the limit value of r_c^h / R

386 into Equation 35.

$$387 \quad p_{limit} = k[1+\ln(\frac{G}{k})] - P_\infty^h \quad (39)$$

388 By using Equations 35 and 36, influences of the internal shear stress on the continuous pressure-

389 expansion response and the limit expansion pressure are depicted in Figures 8 and 9, respectively. It is

390 shown that additional shear stresses reduce the required normal pressure during continuous expansions,

391 and the limit expansion pressure declines with increases of the applied shear stresses and decreases of

392 Poisson's ratio. These reductions are due to the additional plastic failure caused by the internal shear

393 stresses. With fully mobilised shear stresses (i.e. m=1), a reduction of 6% of the limit expansion pressure

394 may be produced within the Tresca material, and this influence would be intensified in materials with

395 greater interface shear stress holding capacity. In addition to the stress reorientation effect considered

396 by Bengough, et al. [18], this solution provides an analytical method to further explain the great reduction

397 of soil resistance measured in rotating CPTs.

7 | ESTIMATION OF MAXIMUM MUD PRESSURE IN HORIZONTAL DIRECTIONAL DRILLINGS

400 In the cavity expansion approach, the maximum mud pressure (p_m) in HDD practices is usually

401 expressed in terms of the maximum allowable plastic radius (R_c). Based on the derived mapping

402 function in Equation 13, p_m in terms of R_c can be expressed as

$$p_m = 2k \ln\left(\frac{R_c}{\delta R}\right) - P_\infty + k\sqrt{1-m^2} + u_0 \tag{40}$$

404 where u_0 is the groundwater pressure at the depth of the borehole.

405 According to Equations 13 and 35, the propagation distance of the plastic failure zone ($r_{c\theta}$) under

406 biaxial stress conditions within the admissible stress range can be expressed as

$$r_{c\theta} = |\omega(\sigma)| = r_c^h \left|(\sigma + \frac{\beta}{\sigma})\right| \tag{41}$$

408 It has been demonstrated that the average cavity displacement in a biaxial stress field can be

409 approximated by the solution derived in the corresponding hydrostatic stress condition [34, 55]. Therefore,

410 the borehole radius pressurised under a uniform mud pressure is estimated by using the displacement

411 solution given in Appendix C. With known initial borehole diameter ($2R_0 = D$) and radius of the

412 elastic-plastic boundary, r_c^h / R can be obtained by letting $r = R$ and $r_0 = R_0$ in Equation C8 as:

$$
\begin{aligned}
&(1-M)^2 - (\frac{R_0}{r_c^h})^2 \\
&= \frac{1}{\varpi^2 - 1}\left[\left(\frac{1+\sqrt{1-m^2(R/r_c^h)^4}}{[1+\sqrt{1-m^2}](R/r_c^h)^2}\right)^\varpi (1+\varpi\sqrt{1-m^2})(\frac{R}{r_c^h})^2 - [1+\varpi\sqrt{1-m^2(R/r_c^h)^4}]\right]
\end{aligned}
\tag{42}
$$

414 Neglecting the internal shear stress, r_c^h / R can be explicitly expressed as:

415 $$\frac{r_c^h}{R} = \left\{ (\varpi - 1)[(1 - \frac{k}{2G})^2 - (\frac{R_0}{r_c^h})^2] + 1 \right\}^{\frac{1}{2(\varpi - 1)}} \quad \text{(special case of } m = 0 \text{)} \tag{43}$$

416 In undrained clays, the plastic volumetric change under loading is often negligible. Therefore, the

417 displacement solution can be further simplified to the Delft solution in this case[56] as Equation 44.

418 $$\frac{r_c^h}{R} = \left[\frac{k}{G} + (\frac{R_0}{r_c^h})^2 \right]^{-\frac{1}{2}} \quad \text{(special case of } m = 0 \text{ and } \nu = 0.5 \text{)} \tag{44}$$

419 The failure model caused by pressurized drilling fluids in clays is considered to be either tensile or shear

420 failure[57-59]. The limit failure pressure varies with the failure model significantly. In general, the tensile

421 fracture pressure is lower than that with shear failure [17, 58]. The failure model primarily depends on the

422 material strength and stress conditions (e.g. the K_0 effect) within homogenous materials [50, 60]. Both

423 elastic (e.g. Kirsch equations) and elastic-plastic (e.g. Delft solution) cavity expansion solutions are

424 often applied to estimate the limit pressure based on different failure criteria [5, 14, 17, 60]. Based on the

425 cavity expansion analysis, the potential failure models under loading may refer to the discussion given

426 in Section 4. Taking Figure 4 as an example, tensile fracture failure tends to occur within the stress

427 ranges of Zones B and E; shear failure may dominate in the Zone C; and a mixed failure may take place

428 in the Zone D. As discussed earlier, the present stress solution was derived under stress conditions

429 within the Zone C. Therefore, Equations 40, 41, and 42 are preferable for estimating the maximum mud

430 pressure of HDDs implemented under stress conditions within this stress range.

431 For horizontal boreholes excavated at relatively shallow depths, apart from the considered K_0 effect, the

432 free ground surface and soil strength and stress gradient with depths may also influence the failure

433 model. The cavity expansion solutions used for this application were mostly developed in an infinite

434 plane. Therefore, different criteria have been proposed in the cavity expansion approach to estimating

435 the maximum mud pressure during HDDs, for example, the maximum allowable plastic radius criterion

436 [42, 61] and maximum hoop strain criterion [5]. Evaluation of the reliability of these criteria is out of the

437 scope of this paper. Instead, the most commonly adopted maximum allowable plastic radius criterion is

438 followed in this solution.

439   Comparing with the elastic-plastic radius calculated in the corresponding hydrostatic stress condition

440   (Equation 42), a shape factor of $|\sigma + \beta / \sigma|$ is introduced by Equation 41 due to the biaxial in-situ

441   stresses. It is shown in Figure 10 (a) that Equation 41 describes that the plastic zone develops farther in

442   the vertical direction while $K_0 < 1$ (e.g. in normally consolidated or lightly overconsolidated clays),

443   whereas the farthest yielding point is along the horizontal direction before failure while $K_0 > 1$ (e.g.

444   heavily overconsolidated clays). Similar trends have also been reported in numerical and experimental

445   studies [56, 62]. However, it needs to point out that the propagation of the plastic zone in cases of $K_0 > 1$

446   may rapidly extend to the free ground surface at the ultimate failure stage instead of propagating farther

447   in the horizontal direction, and, consequently, caution should be exercised when the maximum

448   allowable plastic radius criterion is applied in this case. Therefore, the following discussion

449   concentrates on the performance of the present solution in cases of $K_0 \leq 1$.

450   Following the failure criterion suggested by the Delft solution, which states that the maximum allowable

451   mud pressure will be reached when the plastic region expands to a distance equalling to half of the

452   burial depth, the new method given by Equations 40-42 is applied to estimate p_m for cases while

453   $K_0 \leq 1$. While $K_0 \leq 1$, the farthest yielding point locates above the crown of the borehole with a centre

454   distance of $R_c = r_c^h (1 - \beta) = 0.5H$. Based on numerical simulation results, Xia and Moore [17] reported

455   that the Delft solution may overestimate the mud pressure by up to 15% while $K_0 < 1$, and better

456   agreements with the numerical results have been achieved by their solution considering the K_0 effect [56].

457   Figure 10 (b) demonstrated that the K_0 effect is also well captured by the present solution in the given

458   stress states. Additionally, it is shown that internal shear stresses may lead to further decreases of the

459   maximum allowable mud pressure. Hence, the ignorance of the internal shear stresses may be another

460   noticeable reason that leads to that the Delft solution generally tends to overestimate p_m in practice [45,

461   47].

462   8 | SUMMARY AND CONCLUSIONS

463   An analytical elastoplastic stress solution was developed for a cylindrical cavity under loading in Tresca

464   materials, subjected to biaxial stresses at infinity and uniform normal and shear stresses on the cavity

465   wall. The solution was derived by three steps: a) plastic stresses were derived by assuming that the

466   plastic zone is statically determinate, b) a conformal mapping function describing the outside elastic

467   region was determined through analysing the stress continuity conditions across the elastic-plastic

468   boundary based on Laurent's decomposition theorem and Harnack's theorem, and c) Kolosov-

469   Muskhelishvili complex potentials for the elastic analysis were obtained by using the Cauchy integral

470   method and Fourier series method. Within the admissible application range, the analytical solution

471   showed excellent agreement with FEM simulations and Galin's solution in the special case without

472   internal shear stresses. It was demonstrated that both the internal shear stress and biaxial in-situ soil

473   stresses have fairly significant influences on the distribution of the plastic zone. It was shown that the

474   elastic-plastic boundary is in an elliptic shape under biaxial stress conditions, whose major axis

475   coincides with the direction of the maximum far-field compression stress under loading on the internal

476   cavity wall. The additional shear stresses extend the plastic region, but apply no influence on the shape

477   of the elastic-plastic boundary. In addition, considering the internal shear stresses, an analytical large

478   strain displacement solution was developed for a cylindrical cavity expanding in a hydrostatic in-situ

479   stress field. The derived stress and displacement solutions were applied to account for the additional

480   influence of the shear stresses generated during rotating CPTs and to estimate the maximum allowable

481   mud pressure of HDDs considering both biaxial in-situ stresses and the possibly generated internal shear

482   stresses.

483   To explain the reduction of the normal soil resistance in rotating CPTs due to the shear stresses

484   generated around the interface, an analytical quasi-static cavity expansion solution was developed by

485   combing the derived static stress solution and the continuous displacement solution. It was found that

486   the internal shear stresses would lead to additional plastic failure in the surrounding soil. As a result,

487   the required normal pressure during expansions and the limit normal expansion pressure decline,

488   depending on the shear stress level. These findings further explained the great reduction of the tip

489 resistance measured in rotating CPTs in addition to the reorientation effect of the interface frictional

490 resistance.

491 Considering the K_0 effect and influences of the shear stresses generated during drillings, a new

492 approximate method for estimating the maximum allowable mud pressure during HDDs was developed.

493 With the same maximum allowable plastic radius as in the Delft solution, the new method predicted

494 lower maximum mud pressures than those by the Delft solution in cases of $K_0 < 1$ and showed that the

495 maximum mud pressure declines with a decreasing value of K_0. These findings are consistent with that

496 reported in numerical simulations. In addition, it was found that the internal shear stresses may also

497 cause a considerable reduction of the maximum mud pressure in HDDs, which suggested that this effect

498 may need to be considered while a significant amount of shear stresses between the rotating drill

499 bit/reamer and the surrounding soil are unavoidably generated during drillings.

Appendix A. Purely elastic stress solutions and expressions of principal stresses [1]

501
$$\sigma_r = P_\infty(1 - \frac{R_0^2}{r^2}) - \tau_\infty(1 + \frac{3R_0^4}{r^4} - \frac{4R_0^2}{r^2})\cos 2\theta - p_{in}\frac{R_0^2}{r^2} \tag{A1}$$

502
$$\sigma_\theta = P_\infty(1 + \frac{R_0^2}{r^2}) + \tau_\infty(1 + \frac{3R_0^4}{r^4})\cos 2\theta + p_{in}\frac{R_0^2}{r^2} \tag{A2}$$

503
$$\tau_{r\theta} = \tau_\infty(1 - \frac{3R_0^4}{r^4} + \frac{2R_0^2}{r^2})\sin 2\theta + mk\frac{R_0^2}{r^2} \tag{A3}$$

504
$$\sigma_1 = \frac{\sigma_r + \sigma_\theta}{2} + \left[(\frac{\sigma_r - \sigma_\theta}{2})^2 + \tau_{r\theta}^2\right]^{1/2} \tag{A4}$$

505
$$\sigma_1 = \frac{\sigma_r + \sigma_\theta}{2} - \left[(\frac{\sigma_r - \sigma_\theta}{2})^2 + \tau_{r\theta}^2\right]^{1/2} \tag{A5}$$

506
$$\sigma_2 = v(\sigma_1 + \sigma_3) \tag{A6}$$

Appendix B. Re-derivation of the mapping function [37]

508 To transform the exterior of the elastic-plastic boundary in the physical plane onto the exterior region

509 of the unit circle in the phase plane, a general form of conformal mapping function is introduced [63] as

510
$$\omega(\zeta) = \alpha'\zeta + \alpha_0' + \sum_{n=1}^{\infty} \frac{\alpha_n'}{\zeta^n} \tag{B1}$$

511   Due to the symmetry of the geometry and stress boundaries, the mapping function $\omega(\zeta)$ has the

512   following features [35].

513     $\omega(\zeta) = -\omega(-\zeta)$, $\omega(\zeta) = \overline{\omega(\bar{\zeta})}$ (B2)

514   As a result, α_0 and coefficients of the even order terms are equal to zero, and remaining coefficients

515   are real numbers. $\omega(\zeta)$ can be rewritten as

516     $$z = x + iy = \omega(\zeta) = \alpha\zeta + \sum_{j=0}^{\infty} \frac{\alpha_{2j+1}}{\zeta^{2j+1}}$$ (B3)

517   By multiplying both sides of Equation 11a with $\dfrac{1}{2\pi i}\dfrac{d\sigma}{\sigma - \zeta}$, a Cauchy integral is established as:

518     $$\frac{1}{2\pi i}\int_\gamma \left[\frac{\bar{\omega}(\sigma^{-1})}{\omega(\sigma)}\Phi'(\sigma) + \Psi(\sigma) \right]\frac{d\sigma}{\sigma - \zeta} = \frac{k}{2\pi i}\int_\gamma \left\langle \frac{\sqrt{[\omega(\sigma)\overline{\omega(\sigma)}]^2 - m^2 R_0^4} + mR_0^2 i}{\omega(\sigma)\overline{\omega(\sigma)}} \right\rangle \frac{\overline{\omega(\sigma)}}{\omega(\sigma)}\frac{d\sigma}{\sigma - \zeta}$$ (B4)

519   The right part of Equation B4 should be bounded at infinity [27, 52], hence terms of $j \geq 1$ in the mapping

520   function vanish as shown in Equation B5.

521     $$\frac{\overline{\omega(\sigma)}}{\omega(\sigma)} = \frac{\bar{\omega}(\sigma^{-1})}{\omega(\sigma)} = \frac{\bar{\alpha}\sigma^{-1} + \bar{\alpha}_1\sigma + \bar{\alpha}_3\sigma^3 + \cdots}{\alpha\sigma + \alpha_1\sigma^{-1} + \alpha_3\sigma^{-3} + \cdots} = \frac{\bar{\alpha}_1}{\alpha} + M(\sigma)$$ (B5)

522   where $M(\sigma)$ is analytic on the exterior of contour γ , and $M(\infty) = 0$. Similarly, we find

523     $$\frac{\bar{\omega}(\sigma^{-1})}{\omega(\sigma)}\Phi'(\sigma) = N(\sigma)$$ (B6)

524   where $N(\sigma)$ is analytic on the exterior of contour γ , and $N(\infty) = 0$.

525   Meanwhile, $\Psi(\sigma)$ is holomorphic in Ω^- (including infinity points). Finally, according to Harnack's

526   theorem [20], integrating Equation B4 along γ from Ω^+ side gives

527     $$\alpha_1 = \bar{\alpha}_1 = \frac{\tau_\infty}{k}\alpha$$ (B7)

528   Therefore, the mapping function is in the form of Equation 13. Detailed knowledge about the complex

529   variable methods in elasticity refers to the references of Muskhelishvili [20] and England [63].

530   **Appendix C. Displacement solution for continuous expansions in a hydrostatic stress field**

531 For a cavity deforms in a hydrostatic initial stress state, the radial displacement during continuous

532 expansions can be obtained by a one-dimensional deformation analysis. Note that Zhou et al.[13] presented

533 an analytical expansion solution for this problem by ideally regarding the material as volumetric

534 incompressible. More generally, a new large-strain displacement solution considering the material

535 compressibility is presented here. The elastic displacement is derived based on the small strain theory,

536 and finite strain definitions are adopted in the plastic deformation analysis [64, 65].

537 During purely elastic expansions, the radial displacement (u_r) can be expressed as

$$u_r = r - r_0 = \frac{p_{in} + P_\infty^h}{2G}(\frac{R}{r})^2 r \tag{C1}$$

539 According to the elastic stress solution (i.e. Equations A1, A2, and A3, ignoring the angle-dependent

540 terms) and the yield criterion (i.e. Equation 5), it is found that a plastic zone starts forming from the

541 inner cavity wall while $p_{in} \geq k\sqrt{1-m^2} - P_\infty^h$. While plastic zone appears, the radial displacement in the

542 outside elastic zone can be obtained by replacing p_{in} with the compression pressure at the elastic-

543 plastic boundary ($p_{r_c^h}$) and R with the radius of the elastic-plastic boundary (r_c^h) in the solution of

544 Equation C1. $p_{r_c^h}$ can be calculated by substituting the elastic stress solution into the yield criterion as

$$p_{r_c^h} = k\sqrt{1 - m^2\left(\frac{R}{r_c^h}\right)^4} - P_\infty^h \tag{C2}$$

546 Then the radial displacement at the elastic-plastic boundary is obtained based on the elastic solution as

$$u_r|_{r=r_c} = \frac{kr_c^h}{2G}\sqrt{1 - m^2\left(\frac{R}{r_c^h}\right)^4} \tag{C3}$$

548 Due to the plastic volumetric strain rate is zero in Tresca materials, the compressibility equation in the

549 plastic region [1] can be expressed as

$$\dot{\varepsilon}_r + \dot{\varepsilon}_\theta = \frac{1-2v}{2G}[\dot{\sigma}_r + \dot{\sigma}_\theta] \tag{C4}$$

551 With the initial stress boundary conditions, integrating Equation C4 gives

$$552 \qquad \varepsilon_r + \varepsilon_\theta = \frac{1-2v}{2G}[\sigma_r + \sigma_\theta - 2P_\infty^h] \tag{C5}$$

553 By adopting the definition of logarithmic strain to characterise the accumulative deformation, the radial

554 strain and circumferential strain respectively are

$$555 \qquad \varepsilon_r = \ln \frac{dr}{dr_0} \quad , \quad \varepsilon_\theta = \ln \frac{r}{r_0} \tag{C6}$$

556 By substituting the plastic stresses and Equation C6 into Equation C5, it gives

$$557 \qquad \ln[\frac{r}{r_0}\frac{dr}{dr_0}] = \varpi \ln\left[\frac{r^2 + \sqrt{r^4 - m^2 R^4}}{(r_c^h)^2 + \sqrt{(r_c^h)^4 - m^2 R^4}}\right] \quad (\text{with } \varpi = \frac{(1-2v)k}{G}) \tag{C7}$$

558 With the use of Equation C3, Equation C7 can be integrated over the interval $[r, r_c^h]$, leading to

$$559 \qquad \left[1 - \frac{k}{2G}\sqrt{1 - m^2\left(\frac{R}{r_c^h}\right)^4}\right]^2 (r_c^h)^2 - r_0^2$$

$$= \frac{1}{\varpi^2 - 1}\left\{\left(\frac{(r_c^h)^2 + \sqrt{(r_c^h)^4 - m^2 R^4}}{r^2 + \sqrt{r^4 - m^2 R^4}}\right)^\varpi (r^2 + \varpi\sqrt{r^4 - m^2 R^4}) - [(r_c^h)^2 + \varpi\sqrt{(r_c^h)^4 - m^2 R^4}]\right\} \tag{C8}$$

560 Now the continuous radial expansion of a cylindrical cavity in a hydrostatic in-situ stress field can be

561 modelled by using Equation C8 without limitation of the deformation level.

ACKNOWLEDGEMENTS

REFERENCES

567 1. Yu HS. Cavity expansion methods in geomechanics. Dordrecht, the Netherlands: Kluwer Academic

568 Publishers; 2000.

569 2. Yu HS. The First James K. Mitchell Lecture: In situ soil testing: from mechanics to interpretation.

570 Geomechanics and Geoengineering: An International Journal. 2006;1 (3): 165-195.

571   3. Randolph MF, Dolwin R, Beck R. Design of driven piles in sand. Geotechnique. 1994;44 (3): 427-

572   448.

573   4. Yu HS, Mitchell JK. Analysis of cone resistance: review of methods. Journal of Geotechnical and

574   Geoenvironmental Engineering. 1998;124 (2): 140-149.

575   5. Keulen B. Maximum allowable pressures during horizontal directional drillings focused on sand.

576   Ph.D. Thesis. Delft, the Netherlands: Delft University of Technology; 2001.

577   6. Marshall AM. Tunnel-pile interaction analysis using cavity expansion methods. Journal of

578   Geotechnical and Geoenvironmental Engineering. 2012;138 (10): 1237-1246.

579   7. Mayne PW, Kulhawy FH. K0- OCR Relationships in Soil. Journal of the Soil Mechanics and

580   Foundations Division. 1982;108 (6): 851-872.

581   8. Mesri G, Hayat T. The coefficient of earth pressure at rest. Canadian Geotechnical Journal. 1993;30

582   (4): 647-666.

583   9. Mckenzie BM, Mullins CE, Tisdall JM, Bengough AG. Root–soil friction: quantification provides

584   evidence for measurable benefits for manipulation of root‐tip traits. Plant, Cell and Environment.

585   2013;36: 1085-1092.

586   10. Sadeghi A, Tonazzini A, Popova L, Mazzolai B. A novel growing device inspired by plant root soil

587   penetration behaviors. PloS one. 2014;9 (2): e90139.

588   11. Whalley WR, Leeds-Harrison PB, Clark LJ, Gowing DJG. Use of effective stress to predict the

589   penetrometer resistance of unsaturated agricultural soils. Soil and Tillage Research. 2005;84 (1): 18-

590   27. 10.1016/j.still.2004.08.003.

591   12. Waldron LJ, Constantin GK. Soil resistance to a slowly moving penetrometer. Soil Science.

592   1970;109 (4): 221-226.

593   13. Zhou H, Liu H, Kong G. Influence of shear stress on cylindrical cavity expansion in undrained

594   elastic–perfectly plastic soil. Géotechnique Letters. 2014;4 (3): 203-210.

595   14. Yanagisawa E, Panah AK. Two dimensional study of hydraulic fracturing criteria in cohesive soils.

596   Soils and Foundations. 1994;34 (1): 1-9.

597   15. Detournay E, John CMS. Design charts for a deep circular tunnel under non-uniform loading. Rock

598   Mechanics and Rock Engineering. 1988;21 (2): 119-137.

599   16. Rao P, Cui J, Li J. Elastoplastic Solutions of Cylindrical Cavity Expansion Considering the K0 $\neq$

600   1. In Geotechnical Special Publication: Advances in Soil Dynamics and Foundation Engineering,

601   ASCE: Shanghai, China 2014; pp 433-443.

602   17. Xia HW, Moore ID. Estimation of maximum mud pressure in purely cohesive material during

603   directional drilling. Geomechanics and Geoengineering: An International Journal. 2006;1 (1): 3-11.

604   18. Bengough AG, Mullins CE, Wilson G. Estimating soil frictional resistance to metal probes and its

605   relevance to the penetration of soil by roots. European Journal of Soil Science. 1997;48 (4): 603-612.

606   19. Bishop RF, Hill R, Mott NF. The theory of indentation and hardness tests. The proceedings of the

607   Physical Society. 1945;57 (3): 147–159.

608   20. Muskhelishvili NI. Some basic problems of the mathematical theory of elasticity. 4th ed.;

609   Groningen, the Netherlands.: P. Noordhoff; 1963.

610   21. Stevenson AC. Complex potentials in two-dimensional elasticity. Proceedings of the Royal Society

611   of London. Series A. Mathematical and Physical Sciences. 1945;184 (997): 129-179.

612   22. Kuznetsov VV. Stress concentration near an elliptical hole in an elastic-plastic plate. International

613   Applied Mechanics. 1972;8 (5): 531-536.

614   23. Ivlev DD. On the determination of displacements in the Galin problem. Journal of Applied

615   Mathematics and Mechanics. 1959;23 (5): 1414-1416.

616   24. Kerchman VI, Erlikhman FM. A variational method of solving an elastic-plastic problem for a body

617   with a circular hole. Journal of Applied Mathematics and Mechanics. 1988;52 (1): 105-110.

618   25. Huang WC. Theoretical study of stress concentrations at circular holes and inclusions in strain

619   hardening materials. International Journal of Solids and Structures. 1972;8 (2): 149-192.

620   26. Bradford IDR, Durban D. Stress and deformation fields around a cylindrical cavity embedded in a

621   pressure-sensitive elastoplastic medium. Journal of Applied Mechanics. 1998;65 (2): 374-379.

622   27. Savin GN. Stress distribution around holes. Washington, D.C.: National Aeronautics and Space

623   Administration; 1970.

624   28. Gao XL, Wei XX, Wang ZK. A general analytical solution of a strain-hardening elasto-plastic plate

625   containing a circular hole subjected to biaxial loading-with applications in pressure vessels.

626   International Journal of Pressure Vessels and Piping. 1991;47 (1): 35-55.

627   29. Lee YS, Gong H. Application of complex variables and pseudo-stress function to power-law

628   materials and stress analysis of single rigid inclusion in power-law materials subjected to simple tension

629   and pure shear. International Journal of Mechanical Sciences. 1987;29 (10): 669-694.

630   30. Galin LA. Plane elastic-plastic problem: plastic regions around circular holes in plates and beams.

631   Prikladnaia Matematika i Mekhanika. 1946;10: 365-386.

632   31. Ochensberger W, Celigoj CC, Ulz MH. Amendment to the Galin plane elastoplastic solution.

633   Journal of Engineering Mechanics. 2013;139 (11): 1658-1662.

634   32. Tokar G. Generalization of Galin's problem to frictional materials and discontinuous stress fields.

635   International Journal of Solids and Structures. 1990;26 (2): 129-147.

636   33. Yarushina VM, Dabrowski M, Podladchikov YY. An analytical benchmark with combined pressure

637   and shear loading for elastoplastic numerical models. Geochemistry, Geophysics, Geosystems. 2010;11

638   (8): 1-16. doi:10.1029/2010GC003130.

639   34. Zhou H, Kong G, Liu H. A semi-analytical solution for cylindrical cavity expansion in elastic–

640   perfectly plastic soil under biaxial in situ stress field. Geotechnique. 2016;66 (7): 584-595.

641   35. Detournay E. An approximate statical solution of the elastoplastic interface for the problem of Galin

642   with a cohesive-frictional material. International Journal of Solids and Structures. 1986;22 (12): 1435-

643   1454.

644   36. Cherepanov GP. On a method of solving the elasto-plastic problem. Journal of Applied Mathematics

645   and Mechanics. 1963;27 (3): 644-655.

646   37. Parasyuk OS. An elastic-plastic problem with a non-biharmonic plastic state. Prikladnaya

647   Matematika i Mekhanika. 1948;13: 367-370.

648   38. Zhuang PZ, Yu HS. A unified analytical solution for elastic-plastic stress analysis of a cylindrical

649   cavity in Mohr-Coulomb materials under biaxial in-situ stresses. Geotechnique. 2018.

650   doi.org/10.1680/jgeot.17.P.281.

651 39. Salgado R, Prezzi M. Computation of cavity expansion pressure and penetration resistance in sands.

652 International Journal of Geomechanics. 2007;7 (4): 251-265.

653 40. Salgado R, Mitchell JK, Jamiolkowski M. Cavity expansion and penetration resistance in sand.

654 Journal of Geotechnical and Geoenvironmental Engineering. 1997;123 (4): 344-354.

655 41. Knight M, Duyvestyn G, Gelinas M. Excavation of surface installed pipeline. Journal of

656 infrastructure systems. 2001;7 (3): 123-129.

657 42. Staheli K, Bennett D, O'Donnell HW, Hurley TJ. Installation of pipeline beneath levees using

658 horizontal directional drilling; Technical Report CPAR-GL-98-1. US Army Corps of Engineers:

659 Vicksburg, MS, USA, 1998.

660 43. Adedapo AA. Pavement deterioration and PE pipe behaviour resulting from open-cut and HDD

661 pipeline installation techniques. Ph.D. Thesis. Waterloo, Ontario, Canada: University of Waterloo;

662 2007.

663 44. Bennett D, Wallin K. Step by Step Evaluation of Hydrofracture Risks for HDD Projects. In

664 International Pipelines Conference 2008, Atlanta, GA, 2008.

665 45. Staheli K, Christopher G, Wetter L. Effectiveness of hydrofracture prediction for hdd design. North

666 American Society for Trenchless Technology (NASTT), Chicago, IL. 2010: (F-1-01) 1-10.

667 46. Baumert ME, Allouche EN, Moore ID. Experimental investigation of pull loads and borehole

668 pressures during horizontal directional drilling installations. Canadian geotechnical journal. 2004;41

669 (4): 672-685.

670 47. Rostami A, Yi Y, Bayat A. Estimation of Maximum Annular Pressure during HDD in Noncohesive

671 Soils. International Journal of Geomechanics. 2016;17 (4): 06016029.

672 48. Luger H, Hergarden H. Directional drilling in soft soil: Influence of mud pressures. In Proceedings

673 of the 3rd International Conference on Trenchless Technology-'No Dig 88', Washington D.C., United

674 States, 1988.

675 49. Vesic AS. Expansion of cavities in infinite soil mass. Journal of Soil Mechanics and Foundations

676 Division. 1972;98 (SM3): 265-290.

677 50. Kennedy M, Skinner G, Moore I. Limiting drilling slurry pressures to control hydraulic fracturing

678 during HDD through purely cohesive soil. In 57th Canadian Geotechnical Conference (GeoQuebec

679 2004), Quebec, Canada, 2004; pp 37-44.

680 51. Hill R. The mathematical theory of plasticity. London: Oxford University Press; 1950.

681 52. Chakrabarty J. Theory of plasticity (3rd Ed.). Oxford, UK.: Elsevier Butterworth-Heinemann; 2006.

682 53. Gamelin TW. Complex analysis. New York: Springer; 2001.

683 54. Gibson RE, Anderson WF. In situ measurement of soil properties with the pressuremeter. Civil

684 Engineering and Public Works Review. 1961;56 (658): 615-618.

685 55. Detournay E, Fairhurst C. Two-dimensional elastoplastic analysis of a long, cylindrical cavity under

686 non-hydrostatic loading. International Journal of Rock Mechanics and Mining Sciences &

687 Geomechanics Abstracts. 1987;24 (4): 197-211.

688 56. Xia HW. Investigation of maximum mud pressure within sand and clay during horizontal directional

689 drilling. Ph.D. Thesis. Kingston, Ontario, Canada: Queen's University; 2009.

690 57. Marchi M, Gottardi G, Soga K. Fracturing pressure in clay. Journal of Geotechnical and

691 Geoenvironmental Engineering. 2013;140 (2): 04013008.

692 58. Alfaro MC, Wong RC. Laboratory studies on fracturing of low-permeability soils. Canadian

693 Geotechnical Journal. 2001;38 (2): 303-315.

694 59. Lan H, Moore ID. Practical criteria for assessment of horizontal borehole instability in saturated

695 clay. Tunnelling and Underground Space Technology. 2018;75 (1): 21-35.

696 60. Guo J, He S, Deng Y, Zhao Z. New stress and initiation model of hydraulic fracturing based on

697 nonlinear constitutive equation. Journal of Natural Gas Science and Engineering. 2015;27: 666-675.

698 61. Latorre CA, Wakeley LD, Conroy PJ. Guidelines for installation of utilities beneath corps of

699 engineers levees using horizontal directional drilling; US Army Corps of Engineers, Engineer Research

700 and Development Center: Washington, DC, 2002.

701 62. Yan X, Ma B, Zeng C, Liu Y. Analysis of formation fracturing for the Maxi-HDD Qin River

702 crossing project in China. Tunnelling and Underground Space Technology. 2016;53: 1-12.

703 63. England AH. Complex variable methods in elasticity. Mineola, New York: Dover Publications, Inc;

704 2003.

705   64. Chadwick P. The quasi-static expansion of a spherical cavity in metals and ideal soils. The Quarterly

706   Journal of Mechanics and Applied Mathematics. 1959;12 (1): 52-71.

707   65. Yu HS, Houlsby GT. Finite cavity expansion in dilatant soils: loading analysis. Geotechnique.

708   1991;41 (2): 173-183.

709
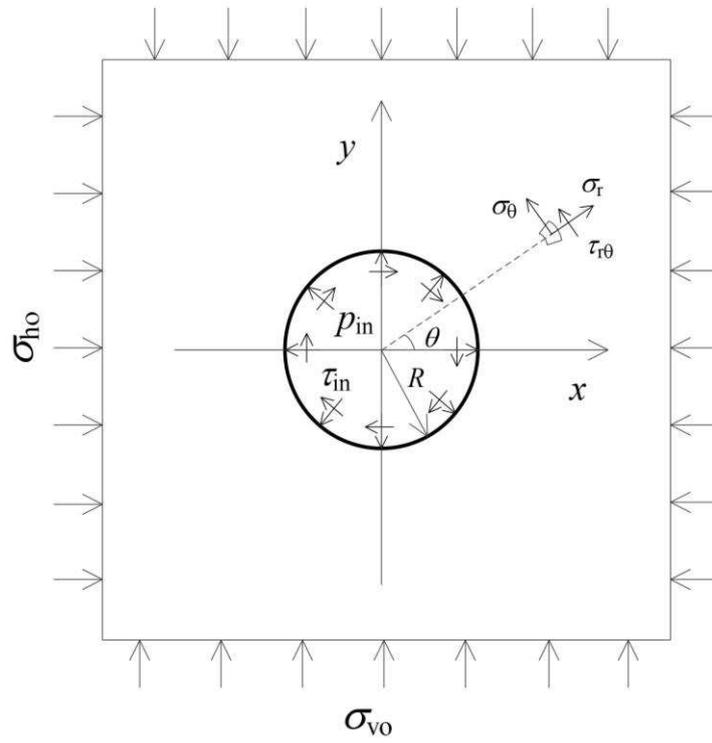
Figures:

Figure 1 Stress boundaries and coordinate systems
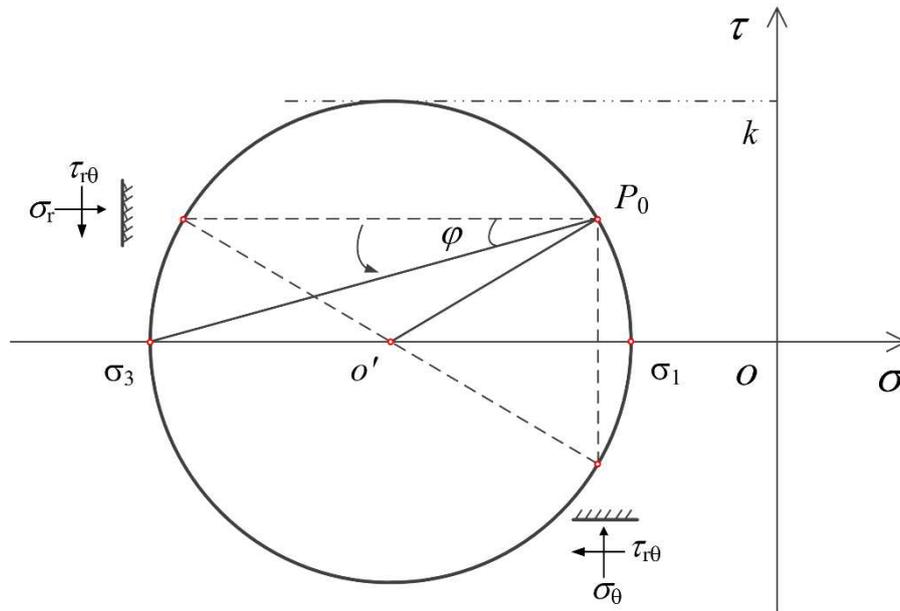
Figure 2 Direction of principal stresses

716
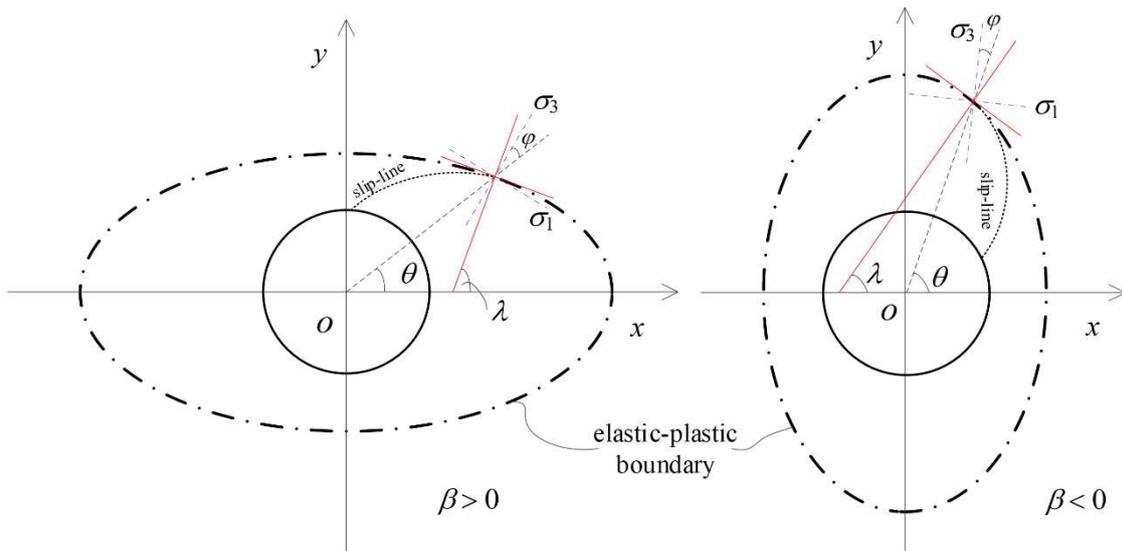
Figure 3 Illustration of slip lines intersecting with the elastic-plastic boundary (taking m>0 as an

example)

719

720
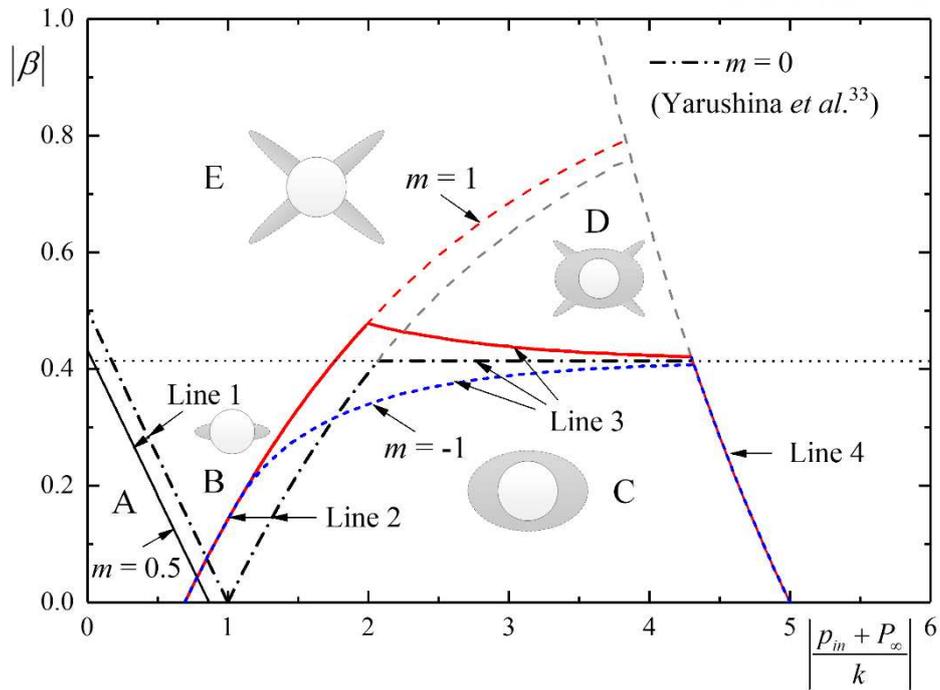
Figure 4 Example limits of different stress states ($\nu = 0.4$)
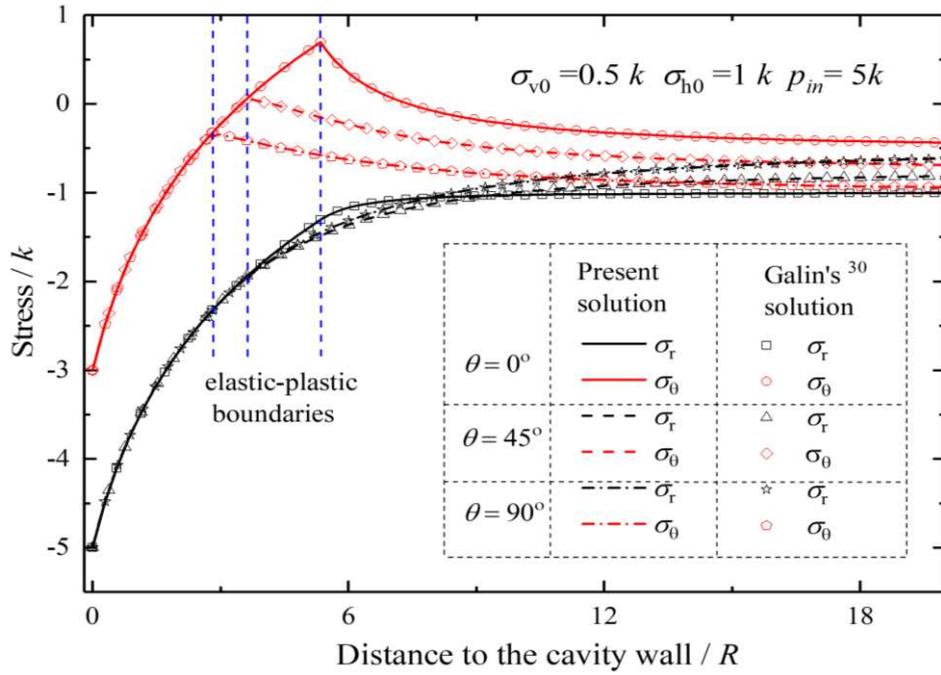
722

723   Figure 5 Comparison between the present solution with m=0 and Galin's [30] solution

724
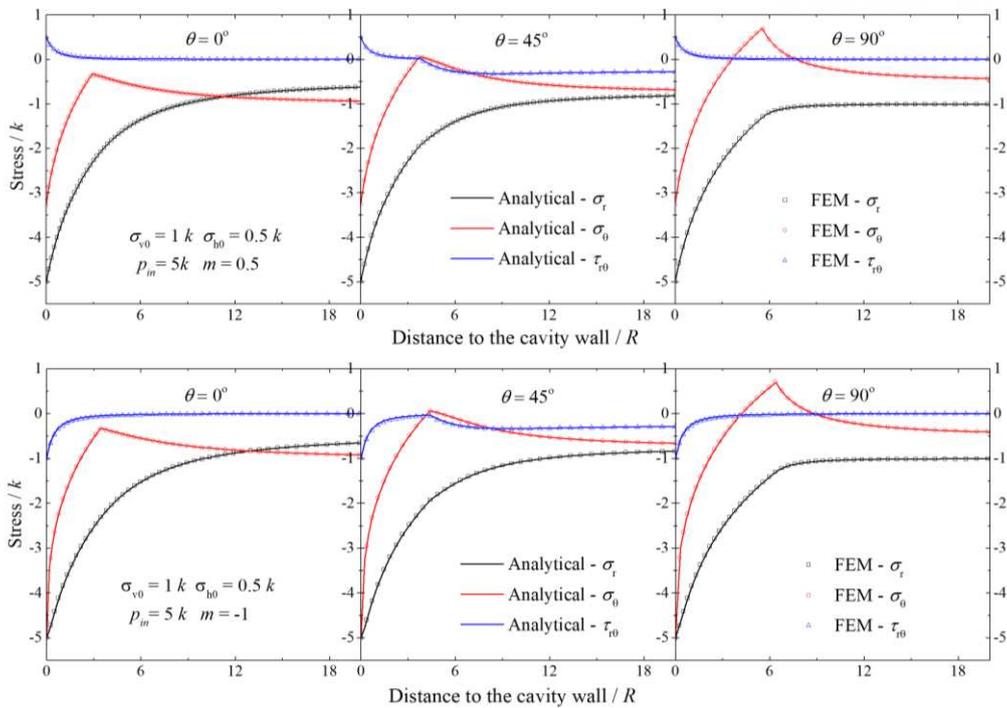
725

726   Figure 6 Comparison of stress components between the analytical solution and FEM simulations

727
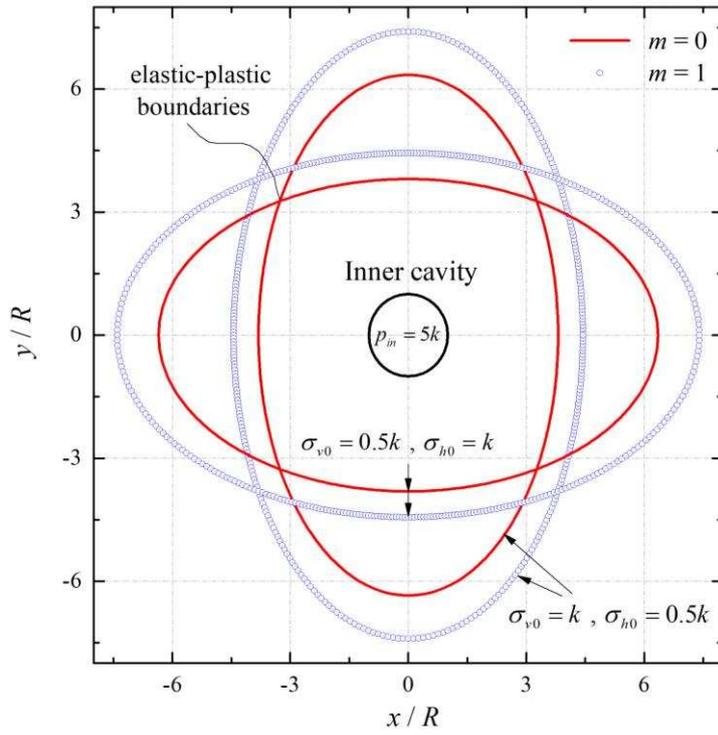
Figure 7 Influences of the internal shear stress and biaxial in-situ stresses on the elastic-plastic

boundary

730


731
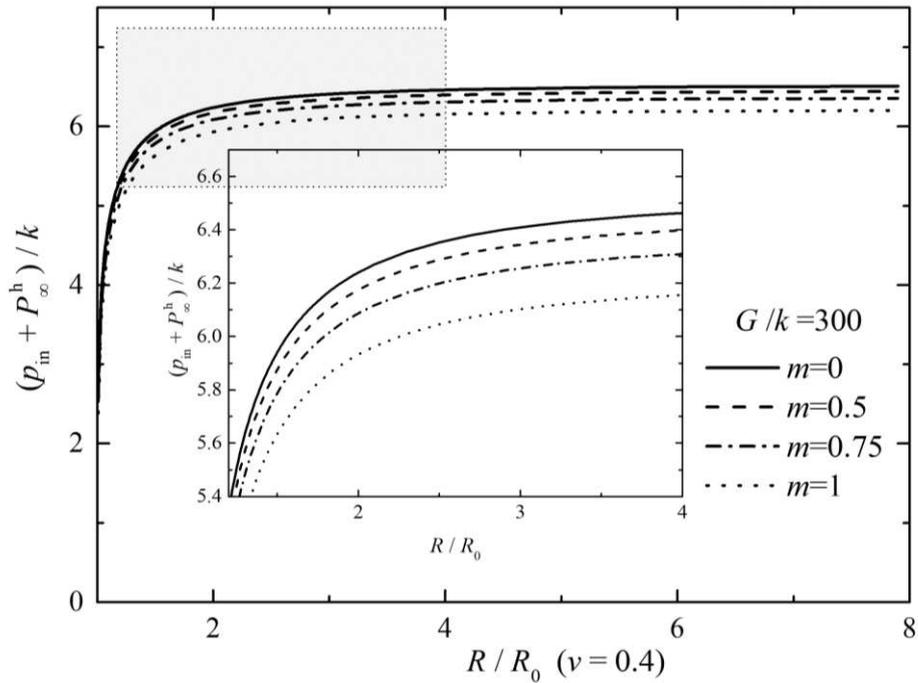
Figure 8 Example continuous pressure-expansion curves

733
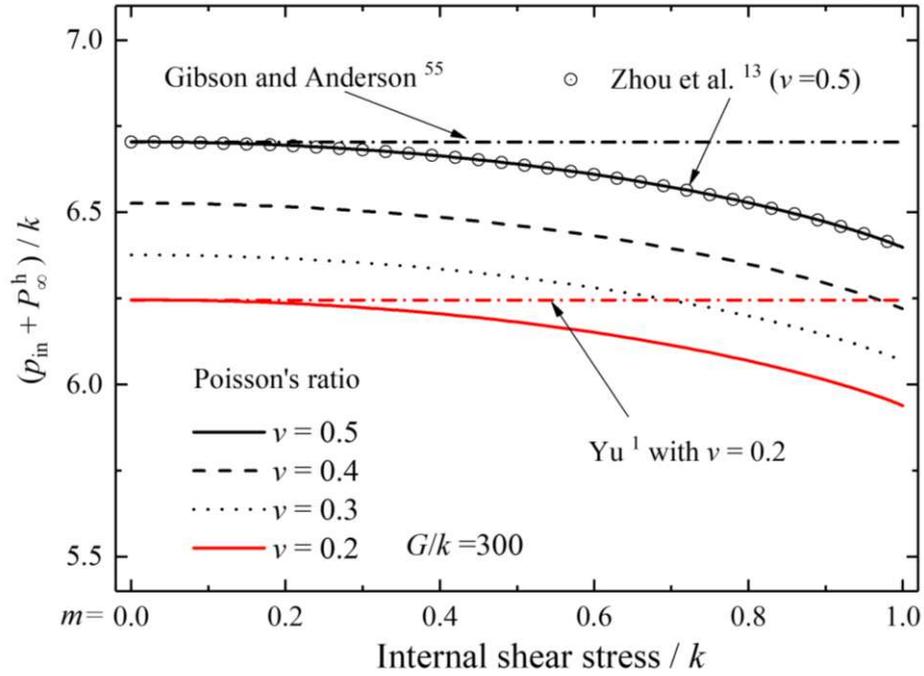
Figure 9 Influences of the internal shear stress on the limit expansion pressure

734

735
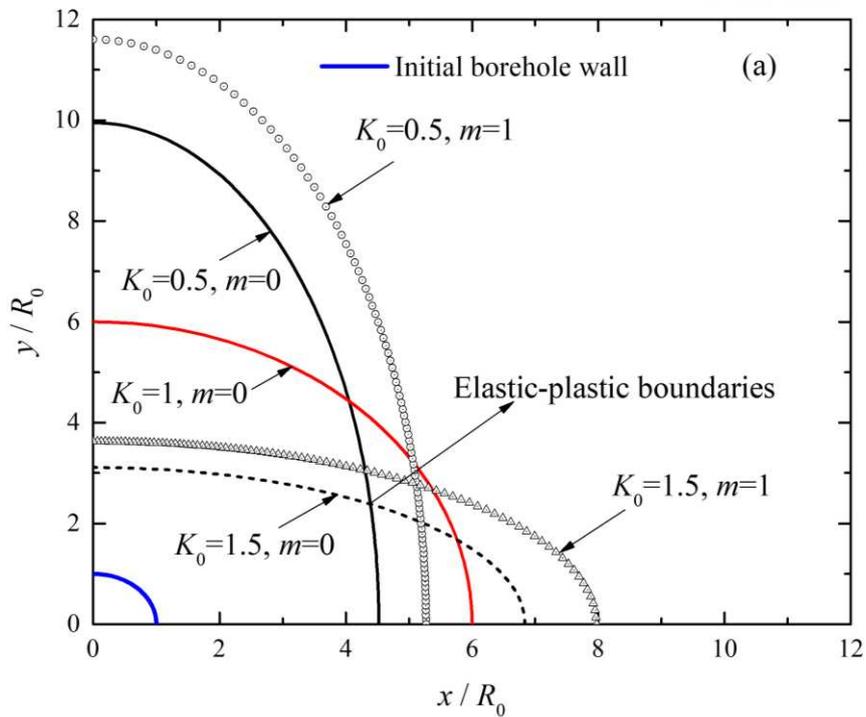
736
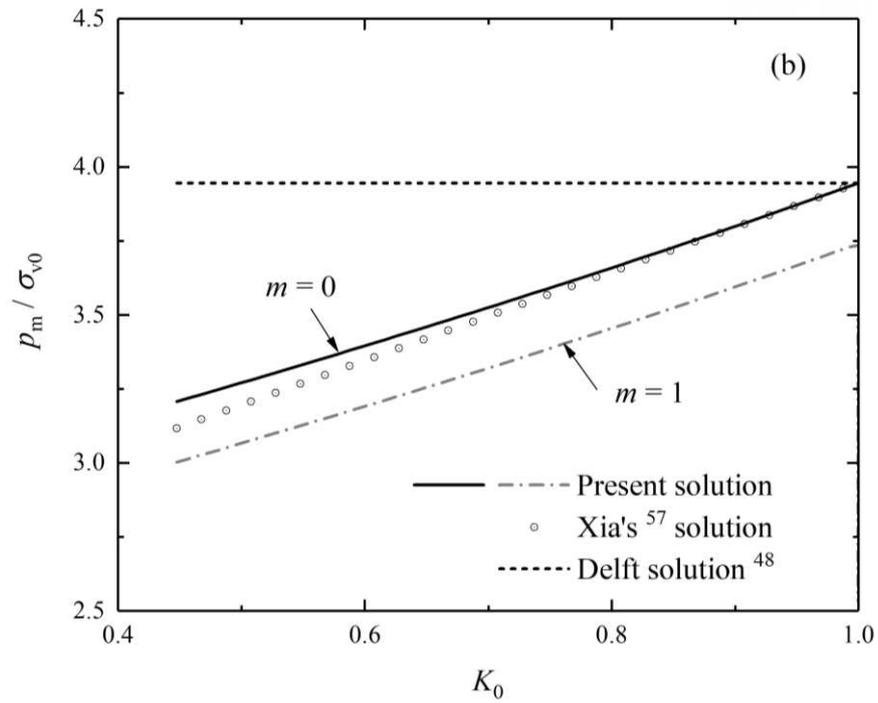
737

738   Figure 10 K_0 effect: (a) elastic-plastic boundaries with the same mud pressure; (b) limit mud pressures

739   with the same value of R_c(=0.5H) (H=3m, D=0.5m, G/k=200, v=0.5, k =40kPa, γ = 20 kN/m^3)